PAPER

Check for updates

Sodium silicate and hexametaphosphate promote the release of (oxyhydr)oxide nanoparticles from corroding iron†

Benjamin F. Trueman, [ID] * Javier Locsin, Evelyne Doré, [ID] Kalli Hood [ID] and Graham A. Gagnon [ID]

Sequestrants such as polyphosphate and sodium silicate are used widely to control iron precipitation in drinking water, but less is known about their impacts on iron corrosion scale. Here we characterize the nanoparticulate iron (oxyhydr)oxide suspensions that result from corroding cast iron coupons in solutions containing either sodium hexametaphosphate (3 mg P L^{-1}) or sodium silicate (100 mg SiO$_2$ L^{-1}). We determined the elemental composition and size distribution of these suspensions using flow field-flow fractionation with ultraviolet, multielement, and multiangle light scattering detection. Both sequestrants yielded stable iron suspensions, and the pooled median radius of gyration at peak ^{57}Fe intensity was 22 nm, corresponding to a sphere-equivalent geometric diameter of 57 nm. The median Feret diameter and ASTM roundness were 50 nm and 0.4, respectively, as determined by transmission electron microscopy. Lead associated readily with iron nanoparticles, and in the hexametaphosphate suspension it associated preferentially with iron over free hexametaphosphate. Sequestrants then, may interact with iron corrosion scale to yield effective transport vectors for lead in drinking water systems, even when complexation of free lead by the sequestrant is negligible.

Environmental significance

Chemical sequestrants—mainly polyphosphate and sodium silicate compounds—improve the appearance of drinking water containing iron and manganese. But polyphosphates in particular have a significant drawback: they increase lead solubility. Here we suggest a different mechanism by which sequestrants might increase lead in drinking water: both hexametaphosphate and sodium silicate disperse (oxyhydr)oxide nanoparticles from corroding iron surfaces. These particles represent potential transport vectors for lead and may increase exposure *via* drinking water.

Introduction

Polyphosphates and sodium silicates are used widely as drinking water additives, often to control aesthetic issues caused by iron from source water and pipe corrosion. These additives have been shown to decrease the colour and turbidity of iron suspensions.[1–5] They reduce particle size, alter morphology, and increase stability by imparting strongly negative zeta potentials.[3–6] There is also evidence from laboratory studies that they control iron corrosion.[7,8]

Less is known about how polyphosphates and silicates impact iron release from corrosion scale. In the short term, an elevated dose of sodium silicate may promote colloidal iron release from corroded iron water mains,[9] but little

characterization of these colloids is available. The effect of polyphosphate on iron colloid release from corrosion scale is also unclear, but it could be important: iron colloids are vectors for trace element transport in drinking water systems, which is particularly relevant for controlling lead in drinking water.[10–12] Moreover, colloidal lead can be difficult to remove at the point of use.[13–15]

Here, we characterize the nanoparticulate iron released from corroding cast iron coupons into solutions containing commonly-used polyphosphate- and silicate-based sequestrants. We determined the concentration and size distribution of colloids (1–1000 nm) and nanoparticles (1–100 nm) using flow field-flow fractionation (FFF) with ultraviolet absorbance, multielement, and multiangle light scattering detectors. We also compare these data with measurements obtained from transmission electron micrographs. We find that both sequestrants yield stable iron nanoparticle suspensions with similar size distributions and that these particles associate readily with lead.

Centre for Water Resources Studies, Department of Civil & Resource Engineering, Dalhousie University, 1360 Barrington St., Halifax, Nova Scotia, Canada, B3H 4R2. E-mail: benjamin.trueman@dal.ca; Fax: +1 902 494 3105; Tel: +1 902 494 6070

Methods

Iron suspensions

To generate each suspension, we submerged two cast iron coupons in 50 mL of solution held inside a 50 mL polypropylene tube with a polyethylene cap (coupons were $76 \times 13 \times 1.5$ mm^3 and sourced from BioSurface Technologies). Immediately before submersion, coupons were polished with 80 and then 400 grit SiC paper.

Each solution contained 35 mg NaHCO$_3$ L^{-1} (5 mg C L^{-1}, Fisher Chemical) and either sodium hexametaphosphate (3 mg P L^{-1}, Alfa Aesar), sodium silicate (100 mg SiO$_2$ L^{-1} with a NaO : SiO$_2$ ratio of 3.22, National Silicates), or no additive (the control suspension). After preparation and mixing, solution pH was adjusted to 7.5 ± 0.2 with HNO$_3$ or NaOH (Fisher Chemical).

Coupons were left to stagnate for 24 hours. Afterward, each suspension was mixed by gentle swirling. Suspensions were then filtered through 0.45 µm cellulose nitrate membrane filters (Whatman) using a syringe-mounted apparatus. To limit adsorption, the first 10 mL of each aliquot was filtered to waste, and the next 20 mL was divided between two smaller polypropylene sample tubes; one for analysis by FFF and the other for direct quantification of the same elements by ICP-MS after acidification to pH < 2 with concentrated trace metal grade HNO$_3$ (Fisher Chemical). To characterize partitioning of lead, we added 200 µg Pb L^{-1} as Pb(NO$_3$)$_2$ (Fisher Chemical) to filtered sodium silicate and hexametaphosphate suspensions. Lead was allowed to react for 53 minutes before analysis by FFF.

Field-flow fractionation

Iron suspensions were fractionated using a modified version of the method described in a recent paper.[11] We used an asymmetric flow FFF system (Postnova AF2000 Multiflow) with a 300 Da poly(ethersulfone) membrane and an autosampler with a 1 mL polyether ether ketone sample loop. The system was coupled sequentially to a UV absorbance detector (Shimadzu SPD-20A), a multiangle light scattering detector (Postnova PN3621), and an ICP-MS (ThermoFisher iCAP-RQ). The mobile phase for all separations was 50 mM tris (hydroxymethyl)aminomethane, adjusted to pH 7.3 with trace metal grade HCl. FFF channel effluent was mixed with internal standards (Sc, In, and Tb) in 2% HNO$_3$ using a mixing tee.

Method parameters are summarized in Table 1. The crossflow was maintained at 2.0 mL min^{-1} for the first 31 minutes of each run (including the focus and transition periods); afterward, it was set to decay linearly over 2 minutes to 0.1 mL min^{-1}. The crossflow was then maintained at 0.1 mL min^{-1} for 10 minutes; afterward it was set to zero for the rinse step (the final 10 minutes of the run).

The deviation of the FFF channel thickness from its nominal value of 500 µm was estimated using a method described elsewhere,[16] using ferritin and bovine serum albumin as globular protein standards with diffusion coefficients drawn from literature.[17,18] The FFF method for the

Table 1 FFF run parameters; since sodium silicate suspensions had much higher iron content, the injection volume was halved

Parameter	Value
Injection volume	0.25 (sodium silicate) and 0.5 mL (hexametaphosphate)
Spacer	500 µm
Total run time	53 min
Detector flow	1 mL min^{-1}
Injection flow	0.2 mL min^{-1}
Focus flow	2.8 mL min^{-1}
Focus period	10 min
Transition period	1 min
Initial crossflow	2 mL min^{-1} (first 31 min of each run)
Crossflow decay	Linear over 2 min
Final crossflow	0.1 mL min^{-1} (10 min)
Rinse step	10 min (no crossflow)

globular protein runs is summarized in Table S1.† The MALS detector was calibrated and normalized using bovine serum albumin, polystyrene sulfonate sodium salt (63.9 kDa), and a mixture of latex particles with nominal geometric diameters of 60, 125, 350 nm.

Inductively coupled plasma mass spectrometry

ICP-MS data were acquired using a ThermoFisher iCAP-RQ operated in kinetic energy discrimination mode with He as the collision gas. We calibrated the ICP-MS on each analysis day using multielement standards in 2% HNO$_3$ at 25, 100, and 250 µg L^{-1}. Standards were introduced to the nebulizer using the ICP-MS autosampler after mixing with FFF channel effluent at the mixing tee. Calibration curves yielded median r^2 values of 0.997 and 1 for ^{31}P and ^{57}Fe.

Quality control spikes in the same matrix (75 µg L^{-1}) yielded median recoveries equaling 99% of ^{31}P and ^{57}Fe. An independently-prepared spike at 40 µg L^{-1} yielded a median ^{57}Fe recovery of 96%. Detection limits were estimated using the 3σ method, with σ calculated separately for the elution step of 5 blanks. Median instantaneous detection limits were estimated at 1.7 and 0.13 µg L^{-1} for ^{31}P and ^{57}Fe.

Transmission electron microscopy (TEM)

At least 13 TEM images were acquired to represent each iron suspension, using a JEOL 1230 instrument. Suspensions were vortexed, and then a 50 µL aliquot from each was loaded onto a 3 mm copper TEM grid (Formvar/Carbon FCF200). Images were scaled and then processed using ImageJ 1.53k (ref. 19) by thresholding to differentiate particles from the background. Two metrics—the Feret diameter (the maximum of all transects across each particle perimeter) and the ASTM roundness[20] (the ratio of the observed area to the area of a circle with a diameter equal to the Feret diameter)—were estimated for each particle. We used a lower cutoff for particle identification of 335 nm^2, which corresponds to the smallest spherical particle that the MALS detector can identify, based on manufacturer specifications (8 nm nominal radius of gyration).

© 2022 The Author(s). Published by the Royal Society of Chemistry

Environ. Sci.: Adv., 2022, **1**, 790–796 | **791**

Data analysis

We analyzed and presented the data using R version 4.2 (ref. 21) and a collection of contributed packages.[22–27] Material necessary to reproduce the results is available on GitHub[28] and functions for post-processing FFF data are available as a separate R package.[29]

Peak fitting

We estimated the fraction of colloidal iron present in each of the two light scattering peaks by fitting a two-peak model to each fractogram. Each peak was represented as a skewed Gaussian and the fractogram as their sum.

Multiangle light scattering

We estimated the radius of gyration (r_g) of iron nanoparticles in each suspension using the Zimm model.[30–34] Specifically, we solved the following equation for r_g^2, the mean squared radius of gyration:

$$\frac{Kc}{R(\theta)} = \frac{1}{M} + \frac{\langle r_g^2 \rangle}{3M}\left[\frac{4\pi\eta_0}{\lambda}\sin\left(\frac{\theta}{2}\right)\right]^2$$

where K is a constant, c and M are the concentration and molar mass of the analyte, respectively, λ is the wavelength of the incident light, θ is the scattering angle, η_0 is the index of refraction of the solvent, and R is the Rayleigh ratio, or the scattering intensity above baseline at each detector angle (Fig. S1 and S2†). For environmental colloids, K, c, and M are

usually unknown, but r_g^2 can be estimated by regressing R^{-1} on $\sin^2(\theta/2)$. That is,

$$\langle r_g^2 \rangle = \frac{3\beta_1\lambda^2}{16\beta_0\pi^2\eta_0^2}$$

where β_0 and β_1 are the intercept and slope of the linear regression. Before fitting the model, data collected at the smallest and largest two scattering angles (7, 12, 156, and 164°) were removed due to excessive noise (Fig. 1).

Results and discussion

Sodium silicate and hexametaphosphate suspensions yielded similar iron fractograms (Fig. 2), with primary and secondary

Fig. 2 Fractograms representing triplicate sodium silicate and hexametaphosphate suspensions and a control suspension (no sequestrant). Theoretical hydrodynamic radius was calculated at constant crossflow (≤31 min retention time), based on channel geometry and flow parameters.[32] Light scattering and absorbance fractograms are displayed with the raw detector responses on the y-axis.
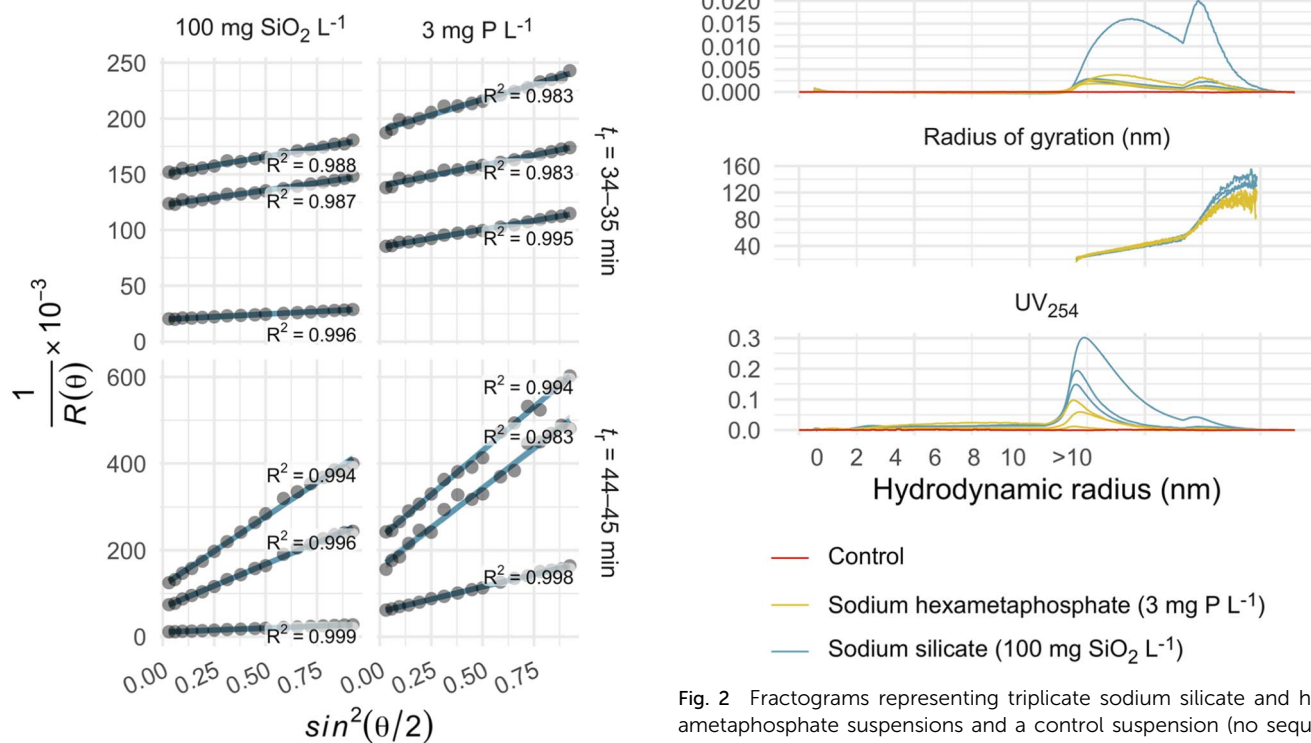

Fig. 1 The Zimm model described the variation in light scattering over the selected range of scattering angles, with r^2 values of 0.983–0.999 (row labels: t_r denotes retention time).

792 | *Environ. Sci.: Adv.*, 2022, **1**, 790–796

© 2022 The Author(s). Published by the Royal Society of Chemistry

light scattering peaks. These peaks had maxima, based on ^{57}Fe intensity, at 34–35 and 44–45 minutes. Iron was also present in a broad peak, eluting between 15 and 30 minutes, that did not coincide with a significant light scattering signal but did adsorb UV light at 254 nm. This peak may represent iron nanoparticles that are too small to be quantified using the online MALS detector.[35] In sodium hexametaphosphate suspensions, the principal ^{31}P peak eluted at approximately 14 minutes, which matches the peak retention of sodium hexametaphosphate in pure water (Fig. S3†).

The control suspension—prepared without sodium silicate or hexametaphosphate—did not contain iron colloids that were detectable by FFF-ICP-MS (Fig. 2). This aligns with research showing that, in the absence of a stabilizing agent—a sequestrant, for instance—iron oxide nanoparticles tend to form aggregates with diameters greater than 450 nm, the upper size limit considered here.[36–38]

The estimated radii of gyration characterizing colloids in the primary and secondary peaks ranged from 22–26 and 70–91 nm in sodium silicate suspensions, and 21–23 and 72–76 nm in hexametaphosphate suspensions (Table 2). While the maximum scattering intensities were similar between the two peaks, the second one accounted for an estimated 5%—or less—of the total iron concentration. This is explained by the much larger particle sizes represented in the secondary peak, and the dependence of scattering intensity on both particle concentration and size.[39,40]

Transmission electron micrograph analysis

We identified 405 and 243 particles in TEM images representing sodium silicate and hexametaphosphate suspensions, respectively, with median Feret diameters of 47 (37–87) and 61 (40–140) nm (Fig. 3, interquartile ranges in parentheses) and roundness values of 0.39 (0.31–0.49) and 0.42 (0.33–0.57) (*i.e.*, "sub-rounded"[20]).

Since suspensions must be evaporated on a grid for TEM analysis, aggregates present in TEM images might be different from the larger particles identified by FFF-MALS. Still, there is an approximate correspondence between the equivalent
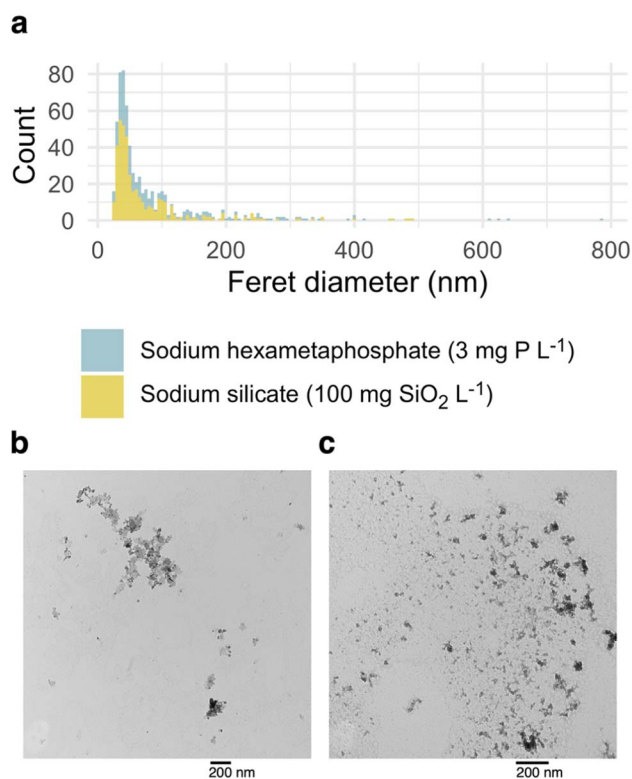

Fig. 3 (a) Histograms representing particles identified in TEM images of sodium silicate and hexametaphosphate-stabilized iron suspensions. (b) A TEM image representing the sodium hexametaphosphate suspension. (c) A TEM image representing the sodium silicate suspension.

spherical diameters obtained from light scattering data and the Feret distances estimated from TEM images, especially for the primary peak at a retention time of 34–35 minutes.

Analyte recovery

We integrated the ^{31}P and ^{57}Fe signals over each fractogram—excluding the focus period—to estimate the concentrations of each analyte. Then, we compared these estimates to the

Table 2 Estimated radii of gyration and calculated geometric (equivalent spherical) diameters of iron colloids. Peaks 1 and 2 eluted at retention times of 34–35 and 44–45 minutes. (N.B., the control suspension did not contain iron colloids detectable by FFF-ICP-MS)

Suspension	Replicate	Peak	Retention time (min)	Radius of gyration (nm)	Spherical equivalent geometric diameter (nm)	% Total Fe (approx.)
Sodium silicate	1	1	35.0	26.3	67.8	80.0
—	—	2	44.5	69.6	180.0	5.5
—	2	1	34.3	21.6	55.7	64.8
—	—	2	45.1	90.6	234.0	2.1
—	3	1	34.2	21.7	56.0	57.9
—	—	2	44.7	78.1	202.0	2.1
Hexametaphosphate	1	1	34.3	20.8	53.8	61.9
—	—	2	44.8	75.0	194.0	3.7
—	2	1	33.8	22.2	57.4	40.9
—	—	2	44.8	72.4	187.0	0.3
—	3	1	34.2	23.2	59.8	44.0
—	—	2	44.9	75.8	196.0	0.5

Environmental Science: Advances

Table 3 Estimated analyte recovery, by suspension type. Since no peaks were identified in fractograms representing the control suspension, recovery of iron by FFF was approximately 0%

Suspension	Analyte	% Recovery	Standard deviation	N
Sodium silicate	^{57}Fe	106.0	3.12	3
Hexametaphosphate	^{31}P	59.9	11.90	3
—	^{57}Fe	46.7	6.59	3

concentrations determined by direct ICP-MS quantification (*i.e.*, no FFF). Recovery of ^{57}Fe was 106 and 46.7% in the sodium silicate and hexametaphosphate suspensions (Table 3).

While FFF recovered essentially all of the iron in sodium silicate suspensions, complexation by polyphosphate species may have resulted in losses of iron to waste in separations of hexametaphosphate suspensions. And since recovery of ^{31}P from a sodium hexametaphosphate standard was 111%, the partial ^{31}P recovery from the iron oxide suspension suggests that hexametaphosphate hydrolyzed to orthophosphate or depolymerized to trimetaphosphate,[41] species that readily pass through the FFF membrane to waste (Fig. S1†). The partial recovery of iron may be due to chelation by trimetaphosphate in particular:[42] the resulting complex would also escape retention by the FFF membrane. In drinking water systems, hexametaphosphate reversion is expected to be significant, especially in older pipe networks.[43]

Potential of colloids for contaminant transport

Lead partitioned readily to suspended iron oxide colloids when added to the sodium silicate and hexametaphosphate suspensions (Fig. 4), with variation in ^{57}Fe explaining $r^2 = 99$ and 93% of variation in ^{208}Pb, respectively. The strong apparent relationship between iron and lead is consistent with research documenting lead adsorption to iron (oxyhydr)oxides[44,45] and, more specifically, elevated lead in iron-rich drinking water.[9,10,46–49] Given that iron colloids with diameters smaller than 450 nm were not detectable in the control suspension, it was excluded from the partitioning experiment. The larger aggregates it contained, though, would also be expected to adsorb lead.[44]

There was little evidence here of lead complexation by free hexametaphosphate: the primary ^{31}P signal at a retention time of approximately 14 minutes did not co-occur with ^{208}Pb. The preferential interaction of lead with iron over hexametaphosphate suggests that the colloids that result from iron corrosion in the presence of a sequestrant may be a particularly effective transport vector for lead. Preferential partitioning of lead to iron (oxyhydr)oxide colloids was reported in a recent paper, where a much larger fraction of total lead was associated with colloidal iron than colloidal dissolved organic matter (although both appeared to bind lead).[11] In another study, a greater fraction of dissolved lead adsorbed to iron oxide particles than precipitated with orthophosphate.[50]

The interaction among corroding iron, sequestrant additives, and lead has important implications for drinking water quality. When polyphosphate or sodium silicate is used to
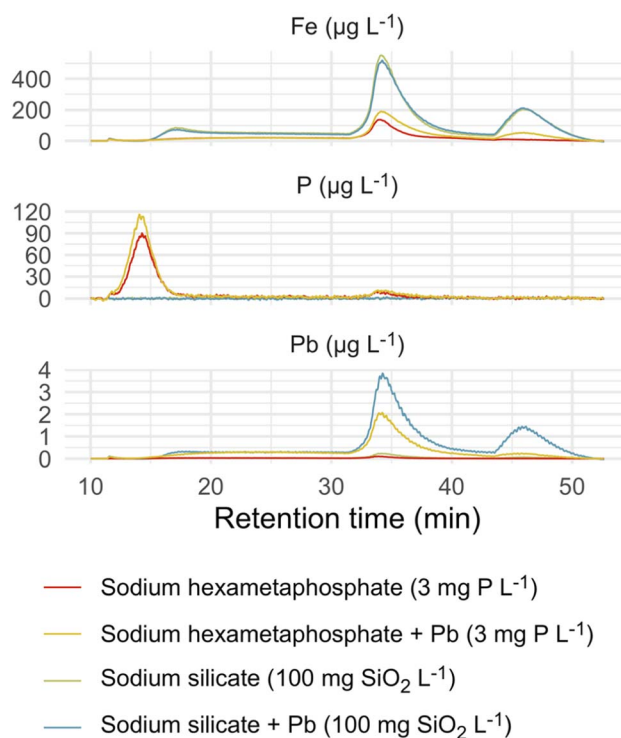

Fig. 4 Fractograms representing sodium silicate and hexametaphosphate suspensions; each is paired with an equivalent suspension dosed with 200 µg Pb L^{-1}. Light scattering and absorbance fractograms are displayed with the raw detector responses on the *y*-axis.

minimize the aesthetic effects of iron corrosion, the iron colloids that result may increase lead mobility. That is, complexation of lead by polyphosphate[51–53] is not the only risk that sequestrant use poses: depending on the relative affinity of lead for the dispersed colloids *versus* the free sequestrant—and the relative concentrations of the two—the dispersion of iron may have a greater effect on lead levels.

Moreover, even sequestrants that do not form strong complexes with lead may increase lead release. In a recent model distribution system study,[9] for instance, an abrupt increase in the dose of sodium silicate was followed by elevated iron release from corroded cast iron pipe sections and lead release from lead pipes downstream. In the long term, silicate treatment may decrease iron release even if it initially does the opposite,[38] but anticipating the short-term effects highlighted here will help protect water quality. Testing that does not account for interactions between lead and iron, then, may underestimate the true risk of elevated lead associated with sequestration.

Conclusion

Sodium silicate and sodium hexametaphosphate solutions yielded nanoparticulate suspensions of iron (oxyhydr)oxide when exposed to a corroding iron surface. The size distributions of the two suspensions were similar, and particle size estimates obtained from light scattering data agreed reasonably well with those determined by TEM image analysis. Lead appeared to

bind to iron nanoparticles, and in the sodium hexametaphosphate suspension it interacted preferentially with iron over free hexametaphosphate. Our findings highlight a risk associated with sequestrant use in drinking water treatment: sequestrants—even those that do not form complexes with lead—may generate colloids that provide an important mobile sink for lead, potentially increasing human exposure.

Author contributions

Benjamin Trueman: investigation, data curation, formal analysis, visualization, writing–original draft; Javier Locsin: investigation, methodology, writing–review & editing; Evelyne Doré: investigation, methodology, writing–review & editing; Kalli Hood: investigation, methodology, writing–review & editing; Graham Gagnon: funding acquisition, writing–review & editing.

Conflicts of interest

There are no conflicts to declare.

Acknowledgements

References

1 R. B. Robinson, R. A. Minear and J. M. Holden, Effects of Several Ions on Iron Treatment by Sodium Silicate and Hypochlorite, *J.–Am. Water Works Assoc.*, 1987, **79**, 116–125.

2 R. B. Robinson, G. D. Reed and B. Frazier, Iron and Manganese Sequestration Facilities Using Sodium Silicate, *J.–Am. Water Works Assoc.*, 1992, **84**, 77–82.

3 D. A. Lytle and V. L. Snoeyink, Effect of ortho-and polyphosphates on the properties of iron particles and suspensions, *J.–Am. Water Works Assoc.*, 2002, **94**, 87–99.

4 M. S. Rahman and G. A. Gagnon, Bench-scale evaluation of drinking water treatment parameters on iron particles and water quality, *Water Res.*, 2014, **48**, 137–147.

5 B. Li, B. F. Trueman, M. S. Rahman, Y. Gao, Y. Park and G. A. Gagnon, Understanding the impacts of sodium silicate on water quality and iron oxide particles, *Environ. Sci.: Water Res. Technol.*, 2019, **5**, 1360–1370.

6 M. L. Magnuson, D. A. Lytle, C. M. Frietch and C. A. Kelty, Characterization of Submicrometer Aqueous Iron(III) Colloids Formed in the Presence of Phosphate by Sedimentation Field Flow Fractionation with Multiangle Laser Light Scattering Detection, *Anal. Chem.*, 2001, **73**, 4815–4820.

7 O. Lahodny-Šarc and L. Kaštelan, The influence of pH on the inhibition of corrosion of iron and mild steel by sodium silicate, *Corros. Sci.*, 1981, **21**, 265–271.

8 M. Koudelka, J. Sanchez and J. Augustyński, On the Nature of Surface Films Formed on Iron in Aggressive and Inhibiting Polyphosphate Solutions, *J. Electrochem. Soc.*, 1982, **129**, 1186–1191.

9 B. Li, B. F. Trueman, S. Munoz, J. A. Locsin and G. A. Gagnon, Impact of sodium silicate on lead release and colloid size distributions in drinking water, *Water Res.*, 2020, 116709.

10 B. F. Trueman and G. A. Gagnon, Understanding the Role of Particulate Iron in Lead Release to Drinking Water, *Environ. Sci. Technol.*, 2016, **50**, 9053–9060.

11 B. F. Trueman, T. Anaviapik-Soucie, V. L'Hérault and G. A. Gagnon, Characterizing colloidal metals in drinking water by field flow fractionation, *Environ. Sci.: Water Res. Technol.*, 2019, **5**, 2202–2209.

12 B. F. Trueman and G. A. Gagnon, A new analytical approach to understanding nanoscale lead-iron interactions in drinking water distribution systems, *J. Hazard. Mater.*, 2016, **311**, 151–157.

13 D. A. Lytle, M. R. Schock, C. Formal, C. Bennett-Stamper, S. Harmon, M. N. Nadagouda, D. Williams, M. K. DeSantis, J. Tully and M. Pham, Lead Particle Size Fractionation and Identification in Newark, New Jersey's Drinking Water, *Environ. Sci. Technol.*, 2020, **54**, 13672–13679.

14 W. Pan, E. R. Johnson and D. E. Giammar, Lead Phosphate Particles in Tap Water: Challenges for Point-of-Use Filters, *Environ. Sci. Technol. Lett.*, 2021, **8**, 244–249.

15 J. M. Purchase, R. Rouillier, K. J. Pieper and M. Edwards, Understanding Failure Modes of NSF/ANSI 53 Lead-Certified Point-of-Use Pitcher and Faucet Filters, *Environ. Sci. Technol. Lett.*, 2020, **8**, 155–160.

16 A. Litzen, Separation speed, retention, and dispersion in asymmetrical flow field-flow fractionation as functions of channel dimensions and flow rates, *Anal. Chem.*, 1993, **65**, 461–470.

17 G. Clough and C. C. Michel, The role of vesicles in the transport of ferritin through frog endothelium, *J. Physiol.*, 1981, **315**, 127–142.

18 A. K. Gaigalas, J. B. Hubbard, M. McCurley and S. Woo, Diffusion of bovine serum albumin in aqueous solutions, *J. Phys. Chem.*, 1992, **96**, 2355–2359.

19 C. A. Schneider, W. S. Rasband and K. W. Eliceiri, NIH Image to ImageJ: 25 years of image analysis, *Nat. Methods*, 2012, **9**, 671–675.

20 L. Li and M. Iskander, Evaluation of Roundness Parameters in Use for Sand, *J. Geotech. Geoenviron. Eng.*, 2021, **147**, 04021081.

21 R. R Core Team, https://www.R-project.org/.

22 H. Wickham, M. Averick, J. Bryan, W. Chang, L. D. McGowan, R. François, G. Grolemund, A. Hayes, L. Henry, J. Hester, M. Kuhn, T. L. Pedersen, E. Miller, S. M. Bache, K. Müller, J. Ooms, D. Robinson, D. P. Seidel, V. Spinu, K. Takahashi, D. Vaughan, C. Wilke, K. Woo and H. Yutani, Welcome to the tidyverse, *J. Open Source Softw.*, 2019, **4**, 1686.

23 J. Allaire, Y. Xie, J. McPherson, J. Luraschi, K. Ushey, A. Atkins, H. Wickham, J. Cheng, W. Chang and

© 2022 The Author(s). Published by the Royal Society of Chemistry

Environ. Sci.: Adv., 2022, **1**, 790–796 | **795**

R. Iannone, *Rmarkdown*, https://github.com/rstudio/rmarkdown.

24 Y. Xie, J. J. Allaire and G. Grolemund, *R Markdown: the Definitive Guide*, Chapman; Hall/CRC, Boca Raton, Florida, 2018.

25 Y. Xie, C. Dervieux and E. Riederer, *R Markdown Cookbook*, Chapman; Hall/CRC, Boca Raton, Florida, 2020.

26 C. O. Wilke, ggtext, https://CRAN.R-project.org/package=ggtext.

27 K. Müller, Here, https://CRAN.R-project.org/package=here.

28 B. Trueman, *Sodium silicate and hexametaphosphate promote the release of (oxyhydr)oxide nanoparticles from corroding iron*, https://github.com/bentrueman/fff-mals.

29 B. Trueman, *fffprocessr*, https://github.com/bentrueman/fffprocessr.

30 F. v. d. Kammer, M. Baborowski and K. Friese, Field-flow fractionation coupled to multi-angle laser light scattering detectors: Applicability and analytical benefits for the analysis of environmental colloids, *Anal. Chim. Acta*, 2005, **552**, 166–174.

31 P. J. Wyatt, Light scattering and the absolute characterization of macromolecules, *Anal. Chim. Acta*, 1993, **272**, 1–40.

32 M. Baalousha, F. V. D. Kammer, M. Motelica-Heino, H. S. Hilal and P. Le Coustumer, Size fractionation and characterization of natural colloids by flow-field flow fractionation coupled to multi-angle laser light scattering, *J. Chromatogr. A*, 2006, **1104**, 272–281.

33 M. P. Petteys and M. E. Schimpf, Characterization of hematite and its interaction with humic material using flow field-flow fractionation, *J. Chromatogr. A*, 1998, **816**, 145–158.

34 J. Gigault, H. El Hadri, S. Reynaud, E. Deniau and B. Grassl, Asymmetrical flow field flow fractionation methods to characterize submicron particles: Application to carbon-based aggregates and nanoplastics, *Anal. Bioanal. Chem.*, 2017, **409**, 6761–6769.

35 C. W. Cuss, I. Grant-Weaver and W. Shotyk, AF4-ICPMS with the 300 Da Membrane To Resolve Metal-Bearing 'Colloids' < 1 kDa: Optimization, Fractogram Deconvolution, and Advanced Quality Control, *Anal. Chem.*, 2017, **89**, 8027–8035.

36 Y. Zhang, Y. Chen, P. Westerhoff and J. Crittenden, Impact of natural organic matter and divalent cations on the stability of aqueous nanoparticles, *Water Res.*, 2009, **43**, 4249–4257.

37 S. E. Mylon, K. L. Chen and M. Elimelech, Influence of Natural Organic Matter and Ionic Composition on the Kinetics and Structure of Hematite Colloid Aggregation: Implications to Iron Depletion in Estuaries, *Langmuir*, 2004, **20**, 9000–9006.

38 J. C. Rushing, L. S. McNeill and M. Edwards, Some effects of aqueous silica on the corrosion of iron, *Water Res.*, 2003, **37**, 1080–1090.

39 B. A. Korgel, J. H. van Zanten and H. G. Monbouquette, Vesicle Size Distributions Measured by Flow Field-Flow Fractionation Coupled with Multiangle Light Scattering, *Biophys. J.*, 1998, **74**, 3264–3272.

40 M. Baalousha, F. V. D. Kammer, M. Motelica-Heino, M. Baborowski, C. Hofmeister and P. Le Coustumer, Size-Based Speciation of Natural Colloidal Particles by Flow Field Flow Fractionation, Inductively Coupled Plasma-Mass Spectroscopy, and Transmission Electron Microscopy/X-ray Energy Dispersive Spectroscopy: Colloids−Trace Element Interaction, *Environ. Sci. Technol.*, 2006, **40**, 2156–2162.

41 R. N. Bell, Hydrolysis of dehydrated Sodium Phosphates, *Ind. Eng. Chem.*, 1947, **39**, 136–140.

42 L. Rasmussen and H. Toftlund, Phosphate compounds as iron chelators in animal cell cultures, *In Vitro Cell. Dev. Biol.*, 1986, **22**, 177–179.

43 T. R. Holm and M. Edwards, Metaphosphate reversion in Laboratory and Pipe-Rig Experiments, *J.–Am. Water Works Assoc.*, 2003, **95**, 172–178.

44 R. McKenzie, The adsorption of lead and other heavy metals on oxides of manganese and iron, *Soil Res.*, 1980, **18**, 61–73.

45 C. C. Ainsworth, P. L. Gassman, J. L. Pilon and W. G. Van Der Sluys, Cobalt, Cadmium, and Lead Sorption to Hydrous Iron Oxide: Residence Time Effect, *Soil Sci. Soc. Am. J.*, 1994, **58**, 1615.

46 B. F. Trueman, G. A. Sweet, M. D. Harding, H. Estabrook, D. P. Bishop and G. A. Gagnon, Galvanic Corrosion of Lead by Iron (Oxyhydr)Oxides: Potential Impacts on Drinking Water Quality, *Environ. Sci. Technol.*, 2017, **51**, 6812–6820.

47 S. Masters and M. Edwards, Increased Lead in Water Associated with Iron Corrosion, *Environ. Eng. Sci.*, 2015, **32**, 361–369.

48 M. McFadden, R. Giani, P. Kwan and S. H. Reiber, Contributions to drinking water lead from galvanized iron corrosion scales, *J.–Am. Water Works Assoc.*, 2011, **103**, 76–89.

49 E. Deshommes, L. Laroche, S. Nour, C. Cartier and M. Prévost, Source and occurrence of particulate lead in tap water, *Water Res.*, 2010, **44**, 3734–3744.

50 Q. Shi, S. Zhang, J. Ge, J. Wei, C. Christodoulatos, G. P. Korfiatis and X. Meng, Lead immobilization by phosphate in the presence of iron oxides: Adsorption versus precipitation, *Water Res.*, 2020, **179**, 115853.

51 T. R. Holm and S. H. Smothers, Characterizing the Lead-Complexing Properties of Polyphosphate Water Treatment Products by Competing-Ligand Spectrophotometry Using 4-(2-Pyridylazo)Resorcinol, *Int. J. Environ. Anal. Chem.*, 1990, **41**, 71–82.

52 T. R. Holm and M. R. Shock, Potential Effects of Polyphosphate Products on Lead Solubility in Plumbing Systems, *J.–Am. Water Works Assoc.*, 1991, **83**, 76–82.

53 M. Edwards and L. S. McNeill, Effect of phosphate inhibitors on lead release from pipes, *J.–Am. Water Works Assoc.*, 2002, **94**, 79–90.